

1

## 2 Modular strategies for spatial mapping of 3 multi-modal mouse brain data

4 Nicholas J. Tustison<sup>1</sup>, Min Chen<sup>2</sup>, Fae N. Kronman<sup>3</sup>, Jeffrey T. Duda<sup>2</sup>, Clare Gamlin<sup>4</sup>, Mia  
5 G. Tustison, Michael Kunst<sup>4</sup>, Rachel Dalley<sup>4</sup>, Staci Sorenson<sup>4</sup>, Quanxin Wang<sup>4</sup>, Lydia Ng<sup>4</sup>,  
6 Yongsoo Kim<sup>3</sup>, and James C. Gee<sup>2</sup>

7 <sup>1</sup>Department of Radiology and Medical Imaging, University of Virginia, Charlottesville, VA

8 <sup>2</sup>Department of Radiology, University of Pennsylvania, Philadelphia, PA

9 <sup>3</sup>Department of Neural and Behavioral Sciences, Penn State University, Hershey, PA

10 <sup>4</sup>Allen Institute for Brain Science, Seattle, WA

11

---

12 Corresponding authors:

13

14 Nicholas J. Tustison, DSc

15 Department of Radiology and Medical Imaging

16 University of Virginia

17 [ntustison@virginia.edu](mailto:ntustison@virginia.edu)

18

19 James C. Gee, PhD

20 Department of Radiology

21 University of Pennsylvania

22 [gee@upenn.edu](mailto:gee@upenn.edu)

<sup>23</sup> **Abstract**

<sup>24</sup> Large-scale efforts by the BRAIN Initiative Cell Census Network (BICCN) are generating a  
<sup>25</sup> comprehensive reference atlas of cell types in the mouse brain. A key challenge in this effort  
<sup>26</sup> is mapping diverse datasets, acquired with varied imaging, tissue processing, and profiling  
<sup>27</sup> methods, into shared coordinate frameworks. Here, we present modular mapping pipelines  
<sup>28</sup> developed using the Advanced Normalization Tools Ecosystem (ANTsX) to align MERFISH  
<sup>29</sup> spatial transcriptomics and high-resolution fMOST morphology data to the Allen Common  
<sup>30</sup> Coordinate Framework (CCFv3), and developmental MRI and LSFM data to the Devel-  
<sup>31</sup> opmental CCF (DevCCF). Simultaneously, we introduce two novel methods: 1) a velocity  
<sup>32</sup> field-based approach for continuous interpolation across developmental timepoints, and 2)  
<sup>33</sup> a deep learning framework for automated brain parcellation using minimally annotated and  
<sup>34</sup> publicly available data. All workflows are open-source and reproducible. We also provide  
<sup>35</sup> general guidance for selecting appropriate strategies across modalities, enabling researchers  
<sup>36</sup> to adapt these tools to new data.

# <sup>37</sup> 1 Introduction

<sup>38</sup> Over the past decade, there have been significant advancements in mesoscopic single-cell  
<sup>39</sup> analysis of the mouse brain. It is now possible to track single neurons<sup>1</sup>, observe whole-  
<sup>40</sup> brain developmental changes at cellular resolution<sup>2</sup>, associate brain regions with genetic  
<sup>41</sup> composition<sup>3</sup>, and locally characterize neural connectivity<sup>4</sup>. These scientific achievements  
<sup>42</sup> have been propelled by high-resolution profiling and imaging techniques that enable sub-  
<sup>43</sup> micron, multimodal, 3D characterizations of whole mouse brains. Among these are micro-  
<sup>44</sup> optical sectioning tomography<sup>5,6</sup>, tissue clearing methods<sup>1,7</sup>, spatial transcriptomics<sup>8,9</sup>, and  
<sup>45</sup> single-cell genomic profiling<sup>10</sup>, each offering expanded specificity and resolution for cell-level  
<sup>46</sup> brain analysis.

<sup>47</sup> Recent efforts by the NIH BRAIN Initiative have mobilized large-scale international collabora-  
<sup>48</sup> tions to create a comprehensive reference database of mouse brain structure and function.  
<sup>49</sup> The BRAIN Initiative Cell Census Network has aggregated over 40 multimodal datasets from  
<sup>50</sup> more than 30 research groups<sup>11</sup>, many of which are registered to standardized anatomical co-  
<sup>51</sup> ordinate systems to support integrated analysis. Among the most widely used of these frame-  
<sup>52</sup> works is the Allen Mouse Brain Common Coordinate Framework (CCFv3)<sup>12</sup>. Other CCFs  
<sup>53</sup> include modality-specific references<sup>13–15</sup> and developmental atlases<sup>16,17</sup> that track structural  
<sup>54</sup> change across time.

## <sup>55</sup> 1.1 Mouse brain mapping challenges

<sup>56</sup> Robust mapping of cell type data into CCFs is essential for integrative analysis of morphology,  
<sup>57</sup> connectivity, and molecular identity. However, each modality poses unique challenges. For  
<sup>58</sup> example, differences in tissue processing, imaging protocols, and anatomical completeness  
<sup>59</sup> often introduce artifacts such as distortion, tearing, holes, and signal dropout<sup>18–23</sup>. Intensity  
<sup>60</sup> differences and partial representations of anatomy can further complicate alignment. Given  
<sup>61</sup> this diversity specialized strategies are often needed to address the unique, modality-specific  
<sup>62</sup> challenges.

<sup>63</sup> Existing mapping solutions fall into three broad categories. The first includes integrated

64 processing platforms that provide users with mapped datasets (e.g., Allen Brain Cell  
65 Atlas<sup>24</sup>, Brain Architecture Portal<sup>25</sup>, OpenBrainMap<sup>26</sup>, and Image and Multi-Morphology  
66 Pipeline<sup>27</sup>). These offer convenience and high-quality curated data, but limited gener-  
67 alizability and customization. The second category involves highly specialized pipelines  
68 tailored to specific modalities such as histology<sup>28–30</sup>, magnetic resonance imaging (MRI)<sup>31–33</sup>,  
69 microCT<sup>34,35</sup>, light sheet fluorescence microscopy (LSFM)<sup>36,37</sup>, fluorescence micro-optical  
70 sectioning tomography (fMOST)<sup>15,38</sup>, and spatial transcriptomics, including multiplexed  
71 error-robust fluorescence in situ hybridization (MERFISH)<sup>39–41</sup>. While effective, these  
72 solutions often require extensive engineering effort to adapt to new datasets or modal-  
73 ities. Finally, general-purpose toolkits such as elastix<sup>42</sup>, Slicer3D<sup>43</sup>, and the Advanced  
74 Normalization Tools Ecosystem (ANTsX)<sup>44</sup> have all been applied to mouse brain mapping  
75 scenarios. These toolkits support modular workflows that can be flexibly composed from  
76 reusable components, offering a powerful alternative to rigid, modality-specific solutions.  
77 However, their use often requires familiarity with pipeline modules, parameter tuning, and  
78 tool-specific conventions which can limit adoption.

79 Building on this third category, we describe a set of modular, ANTsX-based pipelines specif-  
80 ically tailored for mapping diverse mouse brain data into standardized anatomical frame-  
81 works. These include two new pipelines: a velocity field-based interpolation model that  
82 enables continuous transformations across developmental timepoints of the DevCCF, and a  
83 template-based deep learning pipeline for brain extraction and parcellation requiring mini-  
84 mal annotated data. In addition, we include two modular pipelines for aligning multiplexed  
85 error-robust fluorescence in situ hybridization (MERFISH) and fMOST datasets to the Allen  
86 CCFv3. These workflows were adapted and tailored using ANTsX tools to support collabo-  
87 rative efforts within the BICCN and are now made openly available in a reproducible format.  
88 To facilitate broader adoption, we also provide general guidance for customizing these strate-  
89 gies across imaging modalities and data types. We first introduce key components of the  
90 ANTsX toolkit, which provide a basis for all of the mapping workflows described here, and  
91 then detail the specific contributions made in each pipeline.

## **92    1.2 The Advanced Normalization Tools Ecosystem (ANTsX)**

93    The Advanced Normalization Tools Ecosystem (ANTsX) has been used in a number of  
94    applications for mapping mouse brain data as part of core processing steps in various  
95    workflows<sup>30,45–48</sup>, particularly its pairwise, intensity-based image registration capabilities<sup>49</sup>  
96    and bias field correction<sup>50</sup>. Historically, ANTsX development is based on foundational ap-  
97    proaches to image mapping<sup>51–53</sup>, especially in the human brain, with key contributions such  
98    as the Symmetric Normalization (SyN) algorithm<sup>49</sup>. It has been independently evaluated  
99    in diverse imaging domains including multi-site brain MRI<sup>54</sup>, pulmonary CT<sup>55</sup>, and multi-  
100   modal brain tumor registration<sup>56</sup>.

101   Beyond registration, ANTsX provides functionality for template generation<sup>57</sup>, intensity-based  
102   segmentation<sup>58</sup>, preprocessing<sup>50,59</sup>, and deep learning<sup>44</sup>. It has demonstrated strong perfor-  
103   mance in consensus labeling<sup>60</sup>, brain tumor segmentation<sup>61</sup>, and cardiac motion estimation<sup>62</sup>.  
104   Built on the Insight Toolkit (ITK)<sup>63</sup>, ANTsX benefits from open-source contributions while  
105   supporting continued algorithm evaluation and innovation. In the context of mouse brain  
106   data, ANTsX provides a robust platform for developing modular pipelines to map diverse  
107   imaging modalities into CCFs. This paper highlights its use across distinct BICCN projects  
108   such as spatial transcriptomic data from MERFISH, structural data from fMOST, and mul-  
109   timodal developmental data from LSFM and MRI. We describe both shared infrastructure  
110   and targeted strategies adapted to the specific challenges of each modality.

## **111   1.3 Novel ANTsX-based open-source contributions**

112   We introduce two novel contributions to ANTsX developed as part of collabortive efforts  
113   in creating the Developmental Common Coordinate Framework (DevCCF)<sup>16</sup>. First, we  
114   present an open-source velocity field-based interpolation framework for continuous map-  
115   ping across the sampled embryonic and postnatal stages of the DevCCF atlas<sup>16</sup>. This  
116   functionality enables biologically plausible interpolation between timepoints via a time-  
117   parameterized diffeomorphic velocity model<sup>64</sup>, inspired by previous work<sup>65</sup>. Second, we  
118   present a deep learning pipeline for structural parcellation of the mouse brain from mul-

<sup>119</sup> timodal MRI data. This includes two novel components: 1) a template-derived brain ex-  
<sup>120</sup> traction model using augmented data from two ANTsX-derived template datasets<sup>66,67</sup>, and  
<sup>121</sup> 2) a template-derived parcellation model trained on DevCCF P56 labelings mapped from  
<sup>122</sup> the AllenCCFv3. This pipeline demonstrates how ANTsX tools and public resources can be  
<sup>123</sup> leveraged to build robust anatomical segmentation pipelines with minimal annotated data.  
<sup>124</sup> We independently evaluate this framework using a longitudinal external dataset<sup>68</sup>, demon-  
<sup>125</sup> strating generalizability across specimens and imaging protocols. All components are openly  
<sup>126</sup> available through the R and Python ANTsX packages, with general-purpose functionality  
<sup>127</sup> documented in a reproducible, cross-platform tutorial (<https://tinyurl.com/antsxtutorial>).  
<sup>128</sup> Code specific to this manuscript, including scripts to reproduce the novel contributions  
<sup>129</sup> and all associated evaluations, is provided in a dedicated repository (<https://github.com/>  
<sup>130</sup> [ntustison/ANTsXMouseBrainMapping](https://github.com/ntustison/ANTsXMouseBrainMapping)). Additional tools for mapping spatial transcriptomic  
<sup>131</sup> (MERFISH) and structural (fMOST) data to the AllenCCFv3 are separately available at  
<sup>132</sup> (<https://github.com/dontminchenit/CCFAlignmentToolkit>).

133 **2 Results**

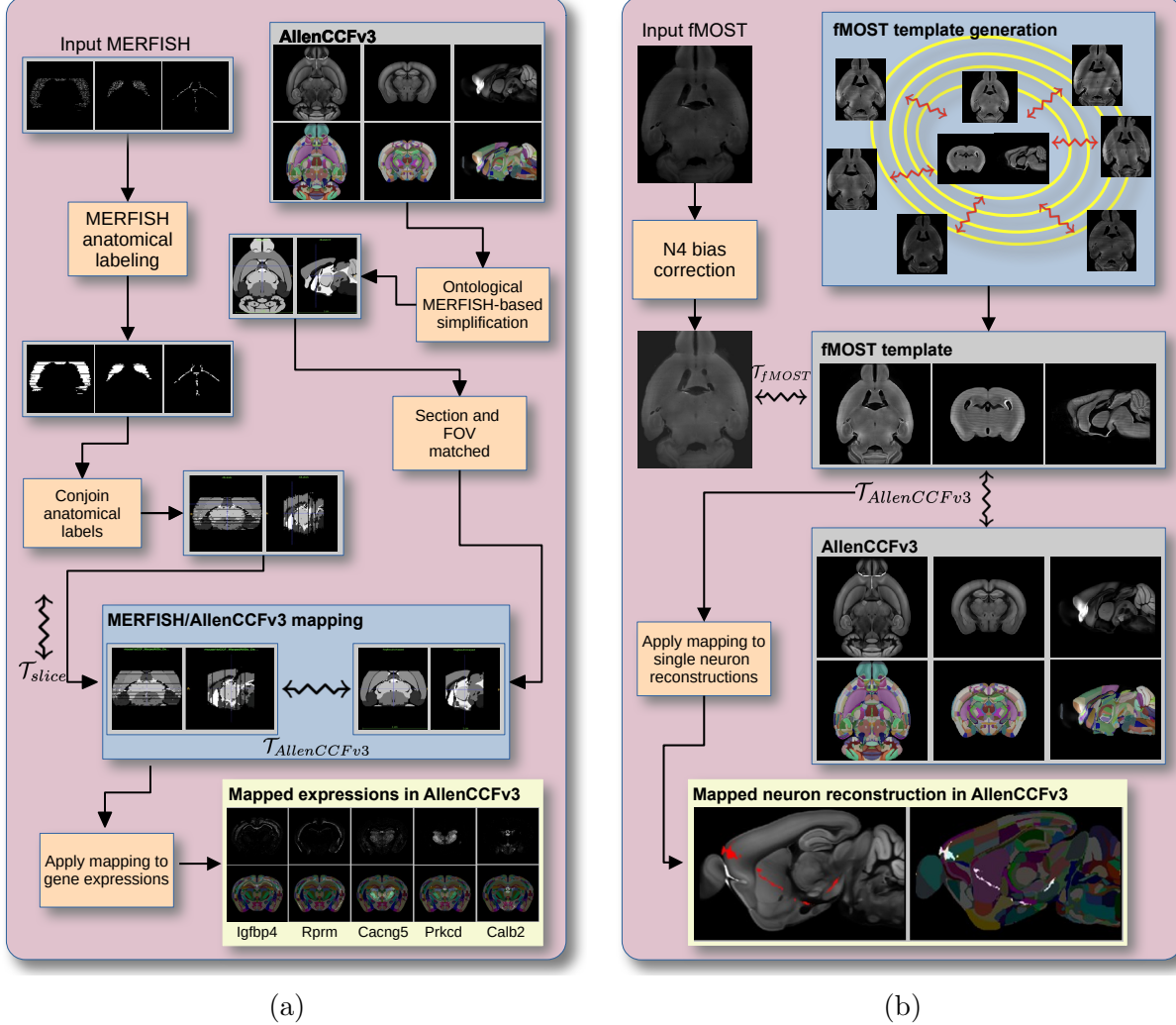


Figure 1: Diagram of the two ANTsX-based pipelines for mapping (a) MERFISH and (b)fMOST data into the space of AllenCCFv3. Each generates the requisite transforms to map individual images to the CCF.

134 **2.1 AllenCCFv3 brain image mapping**

135 **2.1.1 Mapping multiplexed error-robust fluorescence *in situ* hybridization  
136 (MERFISH) data**

137 **Overview.** We developed an ANTsX-based pipeline to map spatial transcriptomic MER-  
138 FISH data into the AllenCCFv3 (Figure 1(a)). This approach was used in recent efforts to

<sup>139</sup> create a high-resolution transcriptomic atlas of the mouse brain<sup>48</sup>. The pipeline maps spa-  
<sup>140</sup> tial gene expression patterns from MERFISH onto anatomical labels in the AllenCCFv3. It  
<sup>141</sup> includes MERFISH-specific preprocessing steps such as section reconstruction, label genera-  
<sup>142</sup> tion from spatial transcriptomic maps, and anatomical correspondence mapping. Alignment  
<sup>143</sup> proceeds in two stages: 1) 3D affine registration and section matching of the AllenCCFv3 to  
<sup>144</sup> the MERFISH data, and 2) linear + deformable 2D section-wise alignment between matched  
<sup>145</sup> MERFISH and atlas slices. These transformations are concatenated to produce a complete  
<sup>146</sup> mapping from each MERFISH data to AllenCCFv3.

<sup>147</sup> **Data.** MERFISH imaging was performed on cryosectioned brains from C57BL/6 mice using  
<sup>148</sup> previously described protocols<sup>48</sup>. Brains were placed into an optimal cutting temperature  
<sup>149</sup> (OCT) compound (Sakura FineTek 4583) stored at -80°. The fresh frozen brain was sectioned  
<sup>150</sup> at 10  $\mu$ m on Leica 3050 S cryostats at intervals of 200  $\mu$ m to evenly cover the brain. A set  
<sup>151</sup> of 500 genes was selected to distinguish  $\sim$  5200 transcriptomic clusters. Raw MERSCOPE  
<sup>152</sup> data were decoded using Vizgen software (v231). Cell segmentation was performed using  
<sup>153</sup> Cellpose<sup>69,70</sup> based on DAPI and PolyT stains which was propagated to adjacent slices across  
<sup>154</sup> z-planes. Each MERFISH cell was assigned a transcriptomic identity by mapping to a  
<sup>155</sup> scRNA-seq reference taxonomy.

<sup>156</sup> **Evaluation.** Alignment quality was evaluated iteratively by an expert anatomist, guided by  
<sup>157</sup> expected gene-marker correspondences to AllenCCFv3 regions. As previously reported<sup>48</sup>, of  
<sup>158</sup> the 554 terminal gray matter regions in the AllenCCFv3, only seven small subregions were  
<sup>159</sup> not represented in the MERFISH dataset: frontal pole layer 1 (FRP1), FRP2/3, FRP5;  
<sup>160</sup> accessory olfactory bulb glomerular (AOBgl), granular (AOBgr), and mitral (AOBmi) layers;  
<sup>161</sup> and the accessory supraoptic group (ASO).

## <sup>162</sup> 2.1.2 Mapping fluorescence micro-optical sectioning tomography (fMOST) data

<sup>163</sup> **Overview.** We also constructed a pipeline for mapping fMOST images to the AllenCCFv3  
<sup>164</sup> using ANTsX (Figure 1(b)). The approach leverages a modality-specific average fMOST  
<sup>165</sup> atlas as an intermediate target, adapted from previous work in human and mouse brain  
<sup>166</sup> mapping<sup>12,15,16,57,71–74</sup>. The atlas was constructed from 30 fMOST images selected to cap-

ture representative variability in anatomical shape and image intensity across the population.  
167 Preprocessing includes cubic B-spline downsampling to match the  $25\text{ }\mu\text{m}$  isotropic AllenC-  
168 CFv3 resolution, stripe artifact suppression using a 3D notch filter implemented with SciPy's  
169 frequency-domain filtering tools, and N4 bias field correction<sup>50</sup>. A one-time, annotation-  
170 driven alignment registers the fMOST atlas to AllenCCFv3 using landmark-based registra-  
171 tion of key structures. This canonical mapping is then reused. New fMOST specimens are  
172 first aligned to the fMOST atlas using standard intensity-based registration, and the con-  
173 catenated transforms yield full spatial normalization to the AllenCCFv3. This same mapping  
174 can be applied to neuron reconstructions to facilitate population-level analysis of morphology  
175 and spatial distribution.  
176

177 **Data.** fMOST imaging was performed on 55 mouse brains with sparse transgenic labeling  
178 of neuron populations<sup>75,76</sup> using the high-throughput fMOST platform<sup>77,78</sup>. Voxel resolution  
179 was  $0.35 \times 0.35 \times 1.0\text{ }\mu\text{m}^3$ . Two imaging channels were acquired: GFP-labeled neuron mor-  
180 phology (green), and propidium iodide counterstaining for cytoarchitecture (red). Alignment  
181 was performed using the red channel for its greater contrast, though multi-channel mapping  
182 is also supported.

183 **Evaluation.** The canonical mapping from the fMOST atlas to AllenCCFv3 was eval-  
184 uated using both quantitative and qualitative approaches. Dice similarity coefficients were  
185 computed between corresponding anatomical labels in the fMOST atlas and AllenCCFv3  
186 following registration. These labels were manually annotated or adapted from existing atlas  
187 segmentations. Representative Dice scores included: whole brain (0.99), caudate putamen  
188 (0.97), fimbria (0.91), posterior choroid plexus (0.93), anterior choroid plexus (0.96), optic  
189 chiasm (0.77), and habenular commissure (0.63). In addition to these quantitative assess-  
190 ments, each registered fMOST specimen was evaluated qualitatively. An expert anatomist  
191 reviewed alignment accuracy and confirmed structural correspondence. Neuron reconstruc-  
192 tions from individual brains were also transformed into AllenCCFv3 space, and their trajec-  
193 tories were visually inspected to confirm anatomical plausibility and preservation of known  
194 projection patterns.

195 **2.2 Continuously mapping the DevCCF developmental trajectory**

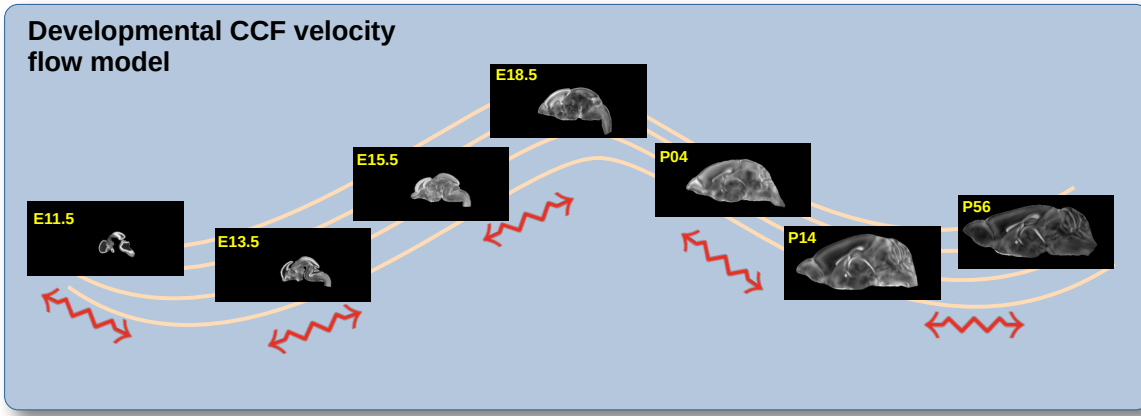


Figure 2: The spatial transformation between any two time points within the continuous DevCCF longitudinal developmental trajectory is available through the use of ANTsX functionality for generating a velocity flow model.

196 The DevCCF is an openly accessible resource for the mouse brain research community<sup>79</sup>,  
197 comprising symmetric, multi-modal MRI and LSFM templates generated using the ANTsX  
198 framework<sup>57</sup>. It spans key stages of mouse brain development (E11.5, E13.5, E15.5, E18.5,  
199 P4, P14, and P56) and includes structural labels defined by a developmental ontology.  
200 The DevCCF was constructed in coordination with the AllenCCFv3 to facilitate integra-  
201 tion across atlases and data types.

202 Although this collection provides broad developmental coverage, its discrete sampling  
203 limits the ability to model continuous transformations across time. To address this,  
204 we developed a velocity flow-based modeling approach that enables anatomically plau-  
205 sible, diffeomorphic transformations between any two continuous time points within  
206 the DevCCF range. This functionality is implemented in both ANTsR and ANTsPy  
207 (`ants.fit_time_varying_transform_to_point_sets(...)`) and integrates seamlessly  
208 with existing ANTsX workflows. The velocity field is encoded as a 4D ITK image where  
209 each voxel stores the  $x,y,z$  components of motion at a given time point.

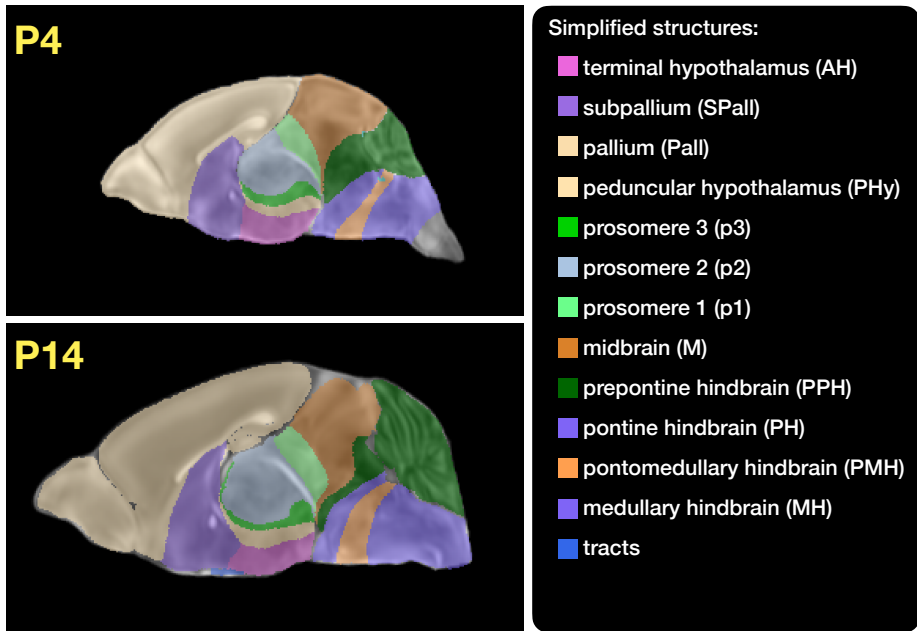


Figure 3: Annotated regions representing common labels across developmental stages, shown for both P4 and P14.

### 210 2.2.1 Data

211 Each DevCCF template includes over 2,500 labeled anatomical regions, with spatial reso-  
212 lutions ranging from  $31.5$  to  $50\mu\text{m}$ . For the velocity flow modeling task, we identified a  
213 common set of 26 bilateral regions (13 per hemisphere) that were consistently labeled across  
214 all timepoints. These regions span major developmental domains including the pallium, sub-  
215 pallium, midbrain, prosomeres, hypothalamus, hindbrain subregions, and key white matter  
216 tracts (Figure 3).

217 Prior to velocity field optimization, all templates were rigidly aligned to the DevCCF P56  
218 template using the centroids of these common label sets. Pairwise correspondence be-  
219 tween adjacent timepoints was then computed using ANTsX's multi-metric registration via  
220 `ants.registration(...)`. Instead of performing intensity-based multi-label registration di-  
221 rectly, we constructed 24 binary label masks per atlas pair (one per structure) and optimized  
222 alignment using the mean squares similarity metric with the SyN transform<sup>49</sup>.

223 To generate the point sets for velocity field optimization, we sampled both boundary (con-  
224 tour) and interior (region) points from the P56 labels and propagated them to each devel-

<sup>225</sup> opmental stage using the learned pairwise transforms. Contours were sampled at 10% of  
<sup>226</sup> available points and regions at 1%, yielding 173,303 total points per atlas ( $N_{contour} = 98,151$ ;  
<sup>227</sup>  $N_{region} = 75,152$ ). Boundary points were assigned double weight during optimization to  
<sup>228</sup> emphasize anatomical boundary correspondence.

## <sup>229</sup> 2.2.2 Velocity field optimization

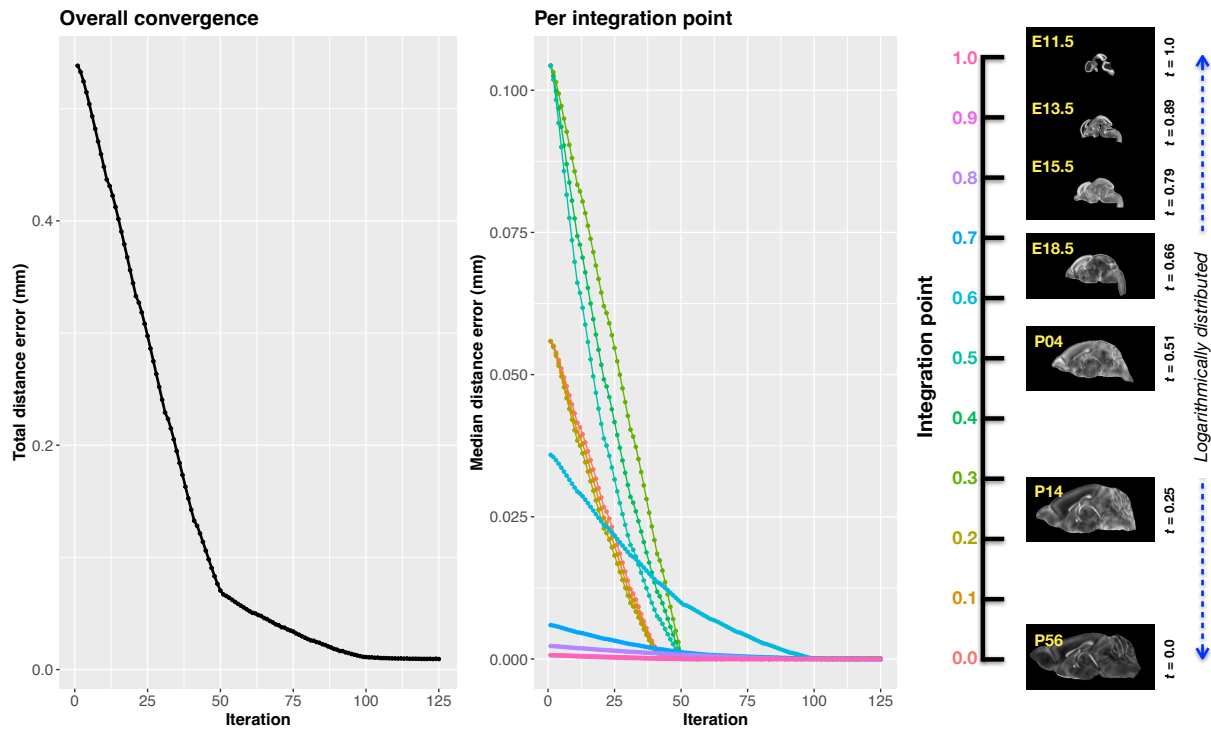


Figure 4: Convergence of velocity field optimization across the DevCCF developmental trajectory. Integration points (color-coded) are distributed along the log-scaled time axis.

<sup>230</sup> The velocity field was optimized using the seven corresponding point sets and their associated  
<sup>231</sup> weights. The field geometry was defined at [256, 182, 360] with 11 integration points at 50  
<sup>232</sup>  $\mu\text{m}$  resolution, yielding a compressed velocity model of  $\sim 2$  GB. This resolution balanced  
<sup>233</sup> accuracy and computational tractability while remaining portable. All data and code are  
<sup>234</sup> publicly available in the accompanying GitHub repository.

<sup>235</sup> To normalize temporal spacing, we assigned scalar values in [0, 1] to each template. Given the  
<sup>236</sup> nonlinear spacing in postnatal development, we applied a logarithmic transform to the raw  
<sup>237</sup> time values prior to normalization. P56 was assigned a span of 28 postnatal days to reflect

known developmental dynamics, which improved the temporal distribution of integration points (Figure 4, right panel).

Optimization was run for a maximum of 200 iterations using a 2020 iMac (3.6 GHz 10-Core Intel Core i9, 64 GB RAM), with each iteration taking  $\sim$  6 minutes. During each iteration, the velocity field was updated across all 11 integration points by computing regularized displacement fields between warped point sets at adjacent time slices. Updates were applied using a step size of  $\delta = 0.2$ . Convergence was assessed via average displacement error across all points, with final convergence achieved after  $\sim$  125 iterations (Figure 4, left panel). Median errors across integration points also trended toward zero, albeit at varying rates.

### 2.2.3 The velocity flow transformation model

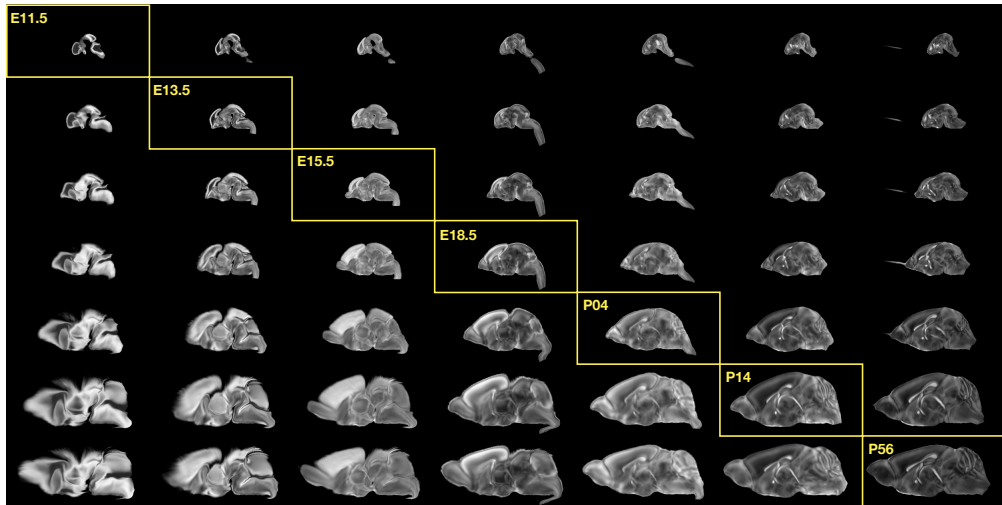


Figure 5: Mid-sagittal visualization of DevCCF templates warped to every other time point. Each row is a reference space; each column is a warped input. Diagonal entries show original templates.

Once optimized, the velocity field enables the computation of diffeomorphic transformations between any pair of continuous time points within the DevCCF developmental range. Figure 5 illustrates cross-warping between all DevCCF stages using the velocity flow model. In addition to facilitating flexible alignment between existing templates, the model also supports the synthesis of virtual templates at intermediate, unsampled developmental stages. As shown in Figure 6, we demonstrate the creation of virtual age templates (e.g., P10.3 and

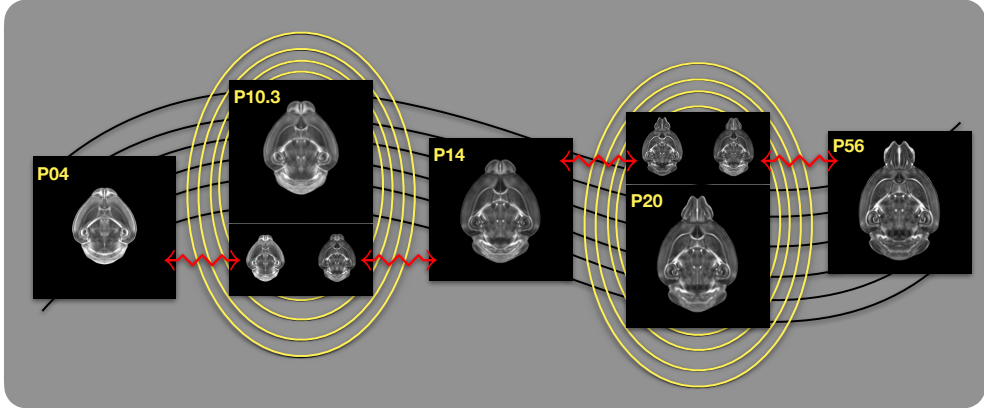


Figure 6: Example of generating “virtual” DevCCF templates at intermediate time points (e.g., P10.3, P20) by warping adjacent stages to a shared time and averaging using ANTsX.

254 P20) by warping adjacent developmental atlases to a target timepoint and constructing an  
 255 averaged representation using ANTsX’s template-building functionality.  
 256 All usage examples, scripts, and supporting data for full reproducibility are publicly available  
 257 in the associated codebase.

### 258 2.3 Automated structural labeling of the mouse brain

259 Structural labeling strategies for the mouse brain are essential for understanding the organi-  
 260 zation and function of the murine nervous system<sup>80</sup>. By dividing the brain into anatomically  
 261 or functionally defined regions, researchers can localize biological processes, relate regional  
 262 features to behavior, or quantify spatial variation in gene expression patterns<sup>81,82</sup>. While  
 263 deep learning techniques have yielded robust segmentation and labeling tools for the hu-  
 264 man brain (e.g., SynthSeg<sup>83</sup>, ANTsXNet<sup>44</sup>), analogous development for mouse data (e.g.,  
 265 MEMOS<sup>84</sup>) has been limited. Mouse neuroimaging often presents unique challenges, such  
 266 as highly anisotropic sampling, that complicate transfer of existing tools. At the same time,  
 267 high resolution resources like the AllenCCFv3 and DevCCF provide reference label sets that  
 268 can serve as training data. We demonstrate how ANTsX can be used to construct a full  
 269 structural labeling pipeline for the mouse brain (Figure 7), including both whole brain seg-  
 270 mentation (i.e., brain extraction) and the subsequent atlas-based region segmentation.

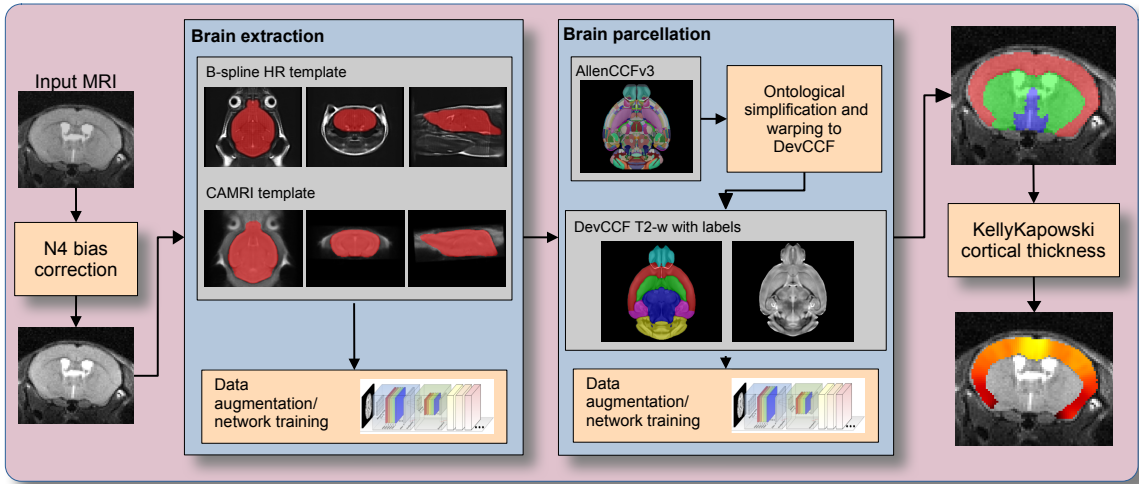


Figure 7: The mouse brain cortical labeling pipeline integrates two deep learning components for brain extraction and anatomical region segmentation. Both networks rely heavily on data augmentation applied to templates constructed from open datasets. The framework also supports further refinement or alternative label sets tailored to specific research needs. Possible applications include voxelwise cortical thickness estimation.

### 2.3.1 Template-based mouse brain extraction network

To develop a general-purpose mouse brain extraction model, we constructed whole-head templates from two publicly available T2-weighted datasets. The first dataset, from the Center for Animal MRI (CAMRI) at the University of North Carolina at Chapel Hill<sup>66</sup>, includes 16 isotropic MRI volumes acquired at  $0.16 \times 0.16 \times 0.16 \text{ mm}^3$  resolution. The second dataset<sup>67</sup> comprises 88 specimens acquired in three orthogonal 2D views (coronal, axial, sagittal) at  $0.08 \times 0.08 \text{ mm}^3$  in-plane resolution with 0.5 mm slice thickness. These orthogonal 2D acquisitions were reconstructed into high-resolution 3D volumes using a B-spline fitting algorithm<sup>85</sup>. Using this synthesized dataset and the CAMRI images, we created two ANTsX-based population templates<sup>57</sup>, each paired with a manually delineated brain mask. These served as the basis for training an initial template-based brain extraction model. Deep learning training of the network employed aggressive data augmentation strategies, including bias field simulation, histogram warping, random spatial deformation, noise injection, and anisotropic resampling. This enabled the model to generalize beyond the two templates. The initial model was released through ANTsXNet and made publicly available.

286 Subsequent community use led to further improvements. A research group applying the  
287 tool to their own ex vivo T2-weighted mouse brain data contributed a third template and  
288 associated mask (acquired at 0.08 mm isotropic resolution). Incorporating this into the  
289 training data improved robustness and accuracy to an independent dataset and extended  
290 the model’s generalizability. The refined model is distributed through ANTsPyNet via  
291 `antspynet.mouse_brain_extraction(...)`.

### 292 2.3.2 Template-based mouse brain anatomical labeling

293 The AllenCCFv3 atlas and its hierarchical ontology, along with the DevCCF, provide a strong  
294 foundation for developing region-wise anatomical labeling models for multi-modal mouse  
295 brain imaging. Using the `allensdk` Python library, we generated a coarse segmentation  
296 scheme by grouping anatomical labels into six major regions: cerebral cortex, cerebral nuclei,  
297 brainstem, cerebellum, main olfactory bulb, and hippocampal formation. These labels were  
298 mapped onto the P56 T2-weighted DevCCF template to serve as training targets. We trained  
299 a 3D U-net–based segmentation network using this template and the same augmentation  
300 strategies described for brain extraction. The model is publicly available via ANTsXNet  
301 (`antspynet.mouse_brain_parcellation(...)`) and supports robust anatomical labeling  
302 across diverse imaging geometries and contrasts. The inclusion of aggressive augmentation,  
303 including simulated anisotropy, enables the model to perform well even on thick-slice input  
304 data. Internally, the model reconstructs isotropic probability and label maps, facilitating  
305 downstream morphometric analyses. For example, this network integrates with the ANTsX  
306 cortical thickness estimation pipeline (`antspynet.mouse_cortical_thickness(...)`) to  
307 produce voxelwise cortical thickness maps, even when applied to anisotropic or limited-  
308 resolution mouse brain data.

### 309 2.3.3 Evaluation

310 For evaluation, we used an additional publicly available dataset<sup>68</sup> that is completely inde-  
311 pendent from the data used in training the brain extraction and parcellation networks. Data  
312 includes 12 specimens each imaged at seven time points (Day 0, Day 3, Week 1, Week 4,

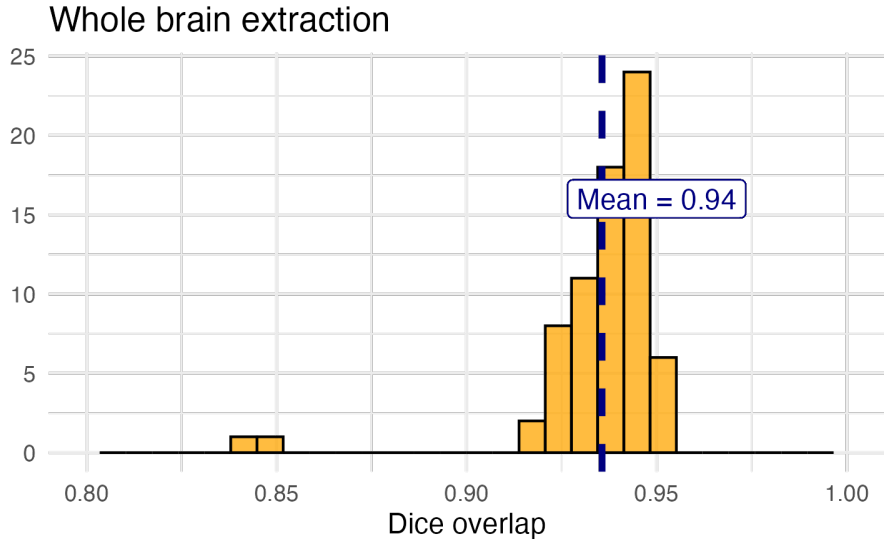
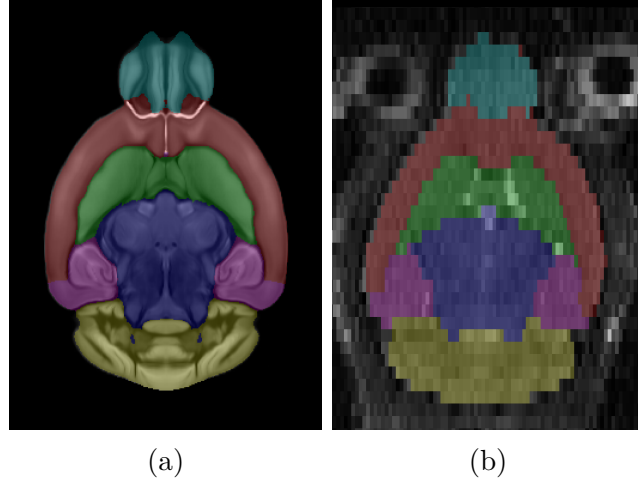


Figure 8: Evaluation of the ANTsX mouse brain extraction on an independent, publicly available dataset consisting of 12 specimens  $\times$  7 time points = 84 total images. Dice overlap comparisons with the user-generated brain masks provide good agreement with the automated results from the brain extraction network.

<sup>313</sup> Week 8, Week 20) with in-house-generated brain masks for a total of 84 images. Spacing is  
<sup>314</sup> anisotropic with an in-plane resolution of  $0.1 \times 0.1 mm^2$  and a slice thickness of  $0.5 mm$ .

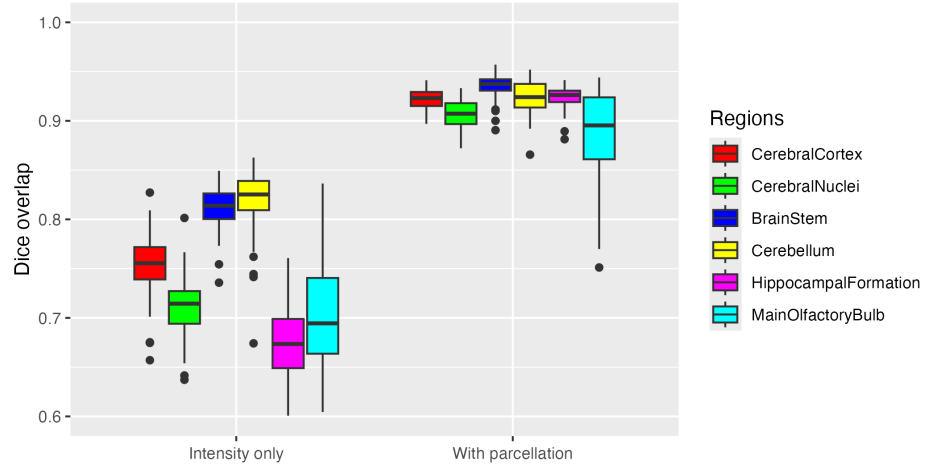
<sup>315</sup> Figure 8 summarizes the whole brain overlap between the provided segmentations for all  
<sup>316</sup> 84 images and the results of applying the proposed network. Also, since mapping to the  
<sup>317</sup> AllenCCFv3 atlas is crucial for many mouse studies, we demonstrate the utility of the second  
<sup>318</sup> network by leveraging the labeled regions to perform anatomically-explicit alignment using  
<sup>319</sup> ANTsX multi-component registration instead of intensity-only registration. For these data,  
<sup>320</sup> the whole brain extraction demonstrates excellent performance across the large age range.  
<sup>321</sup> And although the intensity-only image registration provides adequate alignment, intensity  
<sup>322</sup> with the regional parcellations significantly improves those measures.



(a)

(b)

Normalization to AllenCCFv3



(c)

Figure 9: Evaluation of the ANTsX mouse brain parcellation on the same dataset. (a) T2-w DevCCF P56 with the described parcellation consisting of the cerebral cortex, nuclei, brain stem, cerebellum, main olfactory bulb, and hippocampal formation. (b) Sample subject (NR5 Day 0) with the proposed deep learning-based segmentation. (c) Dice overlap for comparing the regional alignments between registration using intensity information only and using intensity with the given parcellation scheme.

323 **3 Discussion**

324 The diverse mouse brain cell type profiles gathered through BICCN and associated efforts  
325 provide a rich multi-modal resource to the research community. However, despite significant  
326 progress, optimal leveraging of these valuable resources remains an ongoing challenge. A  
327 central component to data integration is accurately mapping novel cell type data into com-  
328 mon coordinate frameworks (CCFs) for subsequent processing and analysis. To meet these  
329 needs, tools for mapping mouse brain data must be both broadly accessible and capable of  
330 addressing challenges unique to each modality. In this work, we described modular ANTsX-  
331 based pipelines developed to support three distinct BICCN efforts encompassing spatial  
332 transcriptomic, morphological, and developmental data. We demonstrated how a flexible  
333 image analysis toolkit like ANTsX can be tailored to address specific modality-driven con-  
334 straints by leveraging reusable, validated components.

335 The MERFISH mapping pipeline illustrates how ANTsX tools can be adapted to accom-  
336 modate high-resolution spatial transcriptomic data. While the general mapping strategy is  
337 applicable to other sectioned histological data, the pipeline includes specific adjustments for  
338 known anatomical and imaging artifacts present in MERFISH datasets. As such, this exam-  
339 ple demonstrates how general-purpose tools can be customized to meet the requirements of  
340 highly specialized data types.

341 The fMOST mapping pipeline was developed with the intention of broader applicability.  
342 Built primarily from existing ANTsX preprocessing and registration modules, this pipeline  
343 introduces an fMOST-specific intermediate atlas to facilitate consistent mappings to the  
344 AllenCCFv3. The use of a canonical fMOST atlas reduces the need for repeated manual  
345 alignment across new datasets, and the resulting transformations can be directly applied to  
346 associated single-neuron reconstructions. This supports integrative morphological analysis  
347 across specimens using a common coordinate system.

348 For developmental data, we introduced a velocity field-based model for continuous interpo-  
349 lation between discrete DevCCF timepoints. Although the DevCCF substantially expands  
350 coverage of developmental stages relative to prior atlases, temporal gaps remain. The ve-

351 locity model enables spatio-temporal transformations within the full developmental interval  
352 and supports the generation of virtual templates at unsampled ages. This functionality is  
353 built using ANTsX components for velocity field optimization and integration, and offers  
354 a novel mechanism for interpolating across the non-linear developmental trajectory of the  
355 mouse brain. Such interpolation has potential utility for both anatomical harmonization and  
356 longitudinal analyses.

357 We also introduced a template-based deep learning pipeline for mouse brain extraction and  
358 parcellation using aggressive data augmentation. This approach is designed to reduce the  
359 reliance on large annotated training datasets, which remain limited in the mouse imaging  
360 domain. Evaluation on independent data demonstrates promising generalization, though  
361 further refinement will be necessary. As with our human-based ANTsX pipelines, failure  
362 cases can be manually corrected and recycled into future training cycles. Community con-  
363 tributions are welcomed and encouraged, providing a pathway for continuous improvement  
364 and adaptation to new datasets.

365 The ANTsX ecosystem offers a powerful foundation for constructing scalable, reproducible  
366 pipelines for mouse brain data analysis. Its modular design and multi-platform support  
367 enable researchers to develop customized workflows without extensive new software devel-  
368 opment. The widespread use of ANTsX components across the neuroimaging community  
369 attests to its utility and reliability. As a continuation of the BICCN program, ANTsX is  
370 well positioned to support the goals of the BRAIN Initiative Cell Atlas Network (BICAN)  
371 and future efforts to extend these mapping strategies to the human brain.

372 **4 Methods**

373 The following methods are all available as part of the ANTsX ecosystem with analogous  
374 elements existing in both ANTsR (ANTs in R) and ANTsPy (ANTs in Python), under-  
375 pinned by a shared ANTs/ITK C++ core. Most development for the work described was  
376 performed using ANTsPy. For equivalent functionality in ANTsR, we refer the reader to the  
377 comprehensive ANTsX tutorial: <https://tinyurl.com/antsxtutorial>.

378 **4.1 General ANTsX utilities**

379 Although focused on distinct data types, the three pipelines presented in this work share  
380 common components that address general challenges in mapping mouse brain data. These  
381 include correcting image intensity artifacts, denoising, spatial registration, template gen-  
382 eration, and visualization. Table 1 provides a concise summary of the relevant ANTsX  
383 functionality.

384 **Preprocessing: bias field correction and denoising.** Standard preprocessing steps in  
385 mouse brain imaging include correcting for spatial intensity inhomogeneities and reducing im-  
386 age noise, both of which can impact registration accuracy and downstream analysis. ANTsX  
387 provides implementations of widely used methods for these tasks. The N4 bias field correction  
388 algorithm<sup>50</sup>, originally developed in ANTs and contributed to ITK, mitigates artifactual, low-  
389 frequency intensity variation and is accessible via `ants.n4_bias_field_correction(...)`.  
390 Patch-based denoising<sup>59</sup> has been implemented as `ants.denoise_image(...)`.

391 **Image registration.** ANTsX includes a robust and flexible framework for pairwise  
392 and groupwise image registration<sup>86</sup>. At its core is the SyN algorithm<sup>49</sup>, a symmetric  
393 diffeomorphic model with optional B-spline regularization<sup>65</sup>. In ANTsPy, registration  
394 is performed via `ants.registration(...)` using preconfigured parameter sets (e.g.,  
395 `antsRegistrationSyNQuick[s]`, `antsRegistrationSyN[s]`) suitable for different imaging  
396 modalities and levels of computational demand. Resulting transformations can be applied  
397 to new images with `ants.apply_transforms(...)`.

Table 1: Sampling of ANTsX functionality

<i>ANTsPy: Preprocessing</i>	
bias field correction	<code>n4_bias_field_correction(...)</code>
image denoising	<code>denoise_image(...)</code>
<i>ANTsPy: Registration</i>	
image registration	<code>registration(...)</code>
image transformation	<code>apply_transforms(...)</code>
template generation	<code>build_template(...)</code>
landmark registration	<code>fit_transform_to_paired_points(...)</code>
time-varying landmark reg.	<code>fit_time_varying_transform_to_point_sets(...)</code>
integrate velocity field	<code>integrate_velocity_field(...)</code>
invert displacement field	<code>invert_displacement_field(...)</code>
<i>ANTsPy: Segmentation</i>	
MRF-based segmentation	<code>atropos(...)</code>
Joint label fusion	<code>joint_label_fusion(...)</code>
diffeomorphic thickness	<code>kelly_kapowski(...)</code>
<i>ANTsPy: Miscellaneous</i>	
Regional intensity statistics	<code>label_stats(...)</code>
Regional shape measures	<code>label_geometry_measures(...)</code>
B-spline approximation	<code>fit_bspline_object_to_scattered_data(...)</code>
Visualize images and overlays	<code>plot(...)</code>
<i>ANTsPyNet: Mouse-specific</i>	
brain extraction	<code>mouse_brain_extraction(...modality="t2"...)</code>
brain parcellation	<code>mouse_brain_parcellation(...)</code>
cortical thickness	<code>mouse_cortical_thickness(...)</code>
super resolution	<code>mouse_histology_super_resolution(...)</code>

ANTsX provides state-of-the-art functionality for processing biomedical image data. Such tools, including deep learning networks, support a variety of mapping-related tasks. A more comprehensive listing of ANTsX tools with self-contained R and Python examples is provided as a gist page on GitHub (<https://tinyurl.com/antsxtutorial>).

398 **Template generation.** ANTsX supports population-based template generation through it-  
399 erative pairwise registration to an evolving estimate of the mean shape and intensity reference  
400 space across subjects<sup>57</sup>. This functionality was used in generating the DevCCF templates<sup>16</sup>.  
401 The procedure, implemented as `ants.build_template(...)`, produces average images in  
402 both shape and intensity by aligning all inputs to a common evolving template.

403 **Visualization.** To support visual inspection and quality control, ANTsPy provides flexible  
404 image visualization with `ants.plot(...)`. This function enables multi-slice and multi-  
405 orientation rendering with optional overlays and label maps.

## 406 4.2 Mapping fMOST data to AllenCCFv3

407 **Preprocessing.** Mapping fMOST data into the AllenCCFv3 presents unique challenges due  
408 to its native ultra-high resolution and imaging artifacts common to the fMOST modality.  
409 Each fMOST image can exceed a terabyte in size, with spatial resolutions far exceeding  
410 those of the AllenCCFv3 ( $25\text{ }\mu\text{m}$  isotropic). To reduce computational burden and prevent  
411 resolution mismatch, each fMOST image is downsampled using cubic B-spline interpolation  
412 via `ants.resample_image(...)` to match the template resolution.

413 Stripe artifacts (i.e., periodic intensity distortions caused by nonuniform sectioning or il-  
414 lumination) are common in fMOST and can mislead deformable registration algorithms.  
415 These were removed using a custom 3D notch filter (`remove_stripe_artifact(...)`) im-  
416 plemented in the `CCFAlignmentToolkit` using SciPy frequency domain filtering. The filter  
417 targets dominant stripe frequencies along a user-specified axis in the Fourier domain. In  
418 addition, intensity inhomogeneity across sections, often arising from variable staining or  
419 illumination, was corrected using N4 bias field correction.

420 **Template-based spatial normalization.** To facilitate reproducible mapping, we first  
421 constructed a contralaterally symmetric average template from 30 fMOST brains and their  
422 mirrored counterparts using ANTsX template-building tools. Because the AllenCCFv3 and  
423 fMOST data differ substantially in both intensity contrast and morphology, direct deformable  
424 registration between individual fMOST brains and the AllenCCFv3 was insufficiently robust.

425 Instead, we performed a one-time expert-guided label-driven registration between the aver-  
426 age fMOST template and AllenCCFv3. This involved sequential alignment of seven manually  
427 selected anatomical regions: 1) brain mask/ventricles, 2) caudate/putamen, 3) fimbria, 4)  
428 posterior choroid plexus, 5) optic chiasm, 6) anterior choroid plexus, and 7) habenular  
429 commissure which were prioritized to enable coarse-to-fine correction of shape differences.  
430 Once established, this fMOST-template-to-AllenCCFv3 transform was reused for all subse-  
431 quent specimens. Each new fMOST brain was then registered to the average fMOST tem-  
432 plate using intensity-based registration, followed by concatenation of transforms to produce  
433 the final mapping into AllenCCFv3 space.

434 **Mapping neuron projections.** A key advantage of fMOST imaging is its ability to support  
435 single neuron projection reconstruction across the entire brain<sup>76</sup>. Because these reconstruc-  
436 tions are stored as 3D point sets aligned to the original fMOST volume, we applied the same  
437 composite transform used for image alignment to the point data using ANTsX functional-  
438 ity. This enables seamless integration of cellular morphology data into AllenCCFv3 space,  
439 facilitating comparative analyses across specimens.

### 440 4.3 Mapping MERFISH data to AllenCCFv3

441 **Preprocessing.** MERFISH data are acquired as a series of 2D tissue sections, each com-  
442 prising spatially localized gene expression measurements at subcellular resolution. To enable  
443 3D mapping to the AllenCCFv3, we first constructed anatomical reference images by aggre-  
444 gating the number of detected transcripts per voxel across all probes within each section.  
445 These 2D projections were resampled to a resolution of  $10 \mu m \times 10 \mu m$  to match the in-plane  
446 resolution of the AllenCCFv3.

447 Sections were coarsely aligned using manually annotated dorsal and ventral midline points,  
448 allowing initial volumetric reconstruction. However, anatomical fidelity remained limited by  
449 variation in section orientation, spacing, and tissue loss. To further constrain alignment and  
450 enable deformable registration, we derived region-level anatomical labels directly from the  
451 gene expression data.

452 **Label creation.** We assigned each detected cell to one of 15 coarse anatomical regions (e.g.,  
453 hippocampus, cortex, striatum—using transcriptomic similarity to scRNA) seq reference  
454 data. These assignments were aggregated across spatial grids to produce probabilistic label  
455 maps for each section. To ensure full regional coverage, morphological dilation was applied to  
456 fill gaps between sparsely distributed cells. Finer-resolution structures (e.g., cortical layers,  
457 habenula) were similarly labeled using marker gene enrichment and spatial constraints. This  
458 dual-level labeling (i.e., coarse and fine) allowed us to construct a robust anatomical scaffold  
459 in the MERFISH coordinate system that could be matched to AllenCCFv3 annotations.

460 **Section matching via global alignment.** A major challenge was compensating for oblique  
461 cutting angles and non-uniform section thickness, which distort the anatomical shape and  
462 spacing of the reconstructed volume. Rather than directly warping the MERFISH data  
463 into atlas space, we globally aligned the AllenCCFv3 to the MERFISH coordinate system.  
464 This was done via an affine transformation followed by resampling of AllenCCFv3 sections  
465 to match the number and orientation of MERFISH sections. This approach minimizes  
466 interpolation artifacts in the MERFISH data and facilitates one-to-one section matching.

467 **Landmark-driven deformable alignment.** We used a 2.5D approach for fine alignment of  
468 individual sections. In each MERFISH slice, deformable registration was driven by sequential  
469 alignment of anatomical landmarks between the label maps derived from MERFISH and  
470 AllenCCFv3. A total of nine regions—including isocortical layers 2/3, 5, and 6, the striatum,  
471 hippocampus, thalamus, and medial/lateral habenula—were registered in an empirically  
472 determined order. After each round, anatomical alignment was visually assessed by an  
473 expert, and the next structure was selected to maximize improvement in the remaining  
474 misaligned regions.

475 The final transform for each section combined the global affine alignment and the per-  
476 structure deformable registrations. These were concatenated to generate a 3D mapping from  
477 the original MERFISH space to the AllenCCFv3 coordinate system. Once established, the  
478 composite mapping enables direct transfer of gene-level and cell-type data from MERFISH  
479 into atlas space, allowing integration with other imaging and annotation datasets.

480 **4.4 DevCCF velocity flow transformation model**

481 The Developmental Common Coordinate Framework (DevCCF)<sup>16</sup> provides a discrete set of  
482 age-specific templates that temporally sample the developmental trajectory. To model this  
483 biological progression more continuously, we introduce a velocity flow-based paradigm for in-  
484 ferring diffeomorphic transformations between developmental stages. This enables anatomi-  
485 cally plausible estimation of intermediate templates or mappings at arbitrary timepoints  
486 between the E11.5 and P56 endpoints of the DevCCF. Our approach builds on established  
487 insights from time-varying diffeomorphic registration<sup>64</sup>, where a velocity field governs the  
488 smooth deformation of anatomical structures over time. Importantly, the framework is ex-  
489 tensible and can naturally accommodate additional timepoints for the potential expansion  
490 of the DevCCF.

491 **Point sampling and region correspondence.** We first coalesced the anatomical labels  
492 across the seven DevCCF templates (E11.5, E13.5, E15.5, E18.5, P4, P14, P56) into 26  
493 common structures that could be consistently identified across development. These include  
494 major brain regions such as the cortex, cerebellum, hippocampus, midbrain, and ventricles.  
495 For each successive pair of templates, we performed multi-label deformable registration us-  
496 ing ANTsX to generate forward and inverse transforms between anatomical label volumes.  
497 From the P56 space, we randomly sampled approximately 1e6 points within and along the  
498 boundaries of each labeled region and propagated them through each pairwise mapping step  
499 (e.g., P56 → P14, P14 → P4, ..., E13.5 → E11.5). This procedure created time-indexed  
500 point sets tracing the spatial evolution of each region.

501 **Velocity field fitting.** Using these point sets, we fit a continuous velocity field over develop-  
502 mental time using a generalized B-spline scattered data approximation method<sup>85</sup>. The field  
503 was parameterized over a log-scaled time axis to ensure finer temporal resolution during early  
504 embryonic stages, where morphological changes are most rapid. Optimization proceeded for  
505 approximately 125 iterations, minimizing the average Euclidean norm between transformed  
506 points at each step. Ten integration points were used to ensure numerical stability. The  
507 result is a smooth, differentiable vector field that defines a diffeomorphic transform between  
508 any two timepoints within the template range.

509 **Applications and availability.** This velocity model can be used to estimate spa-  
510 tial transformations between any pair of developmental stages—even those for which  
511 no empirical template exists—allowing researchers to create interpolated atlases, align  
512 new datasets, or measure continuous structural changes. It also enables developmental  
513 alignment of multi-modal data (e.g., MRI to LSFM) by acting as a unifying spatiotem-  
514 poral scaffold. The underlying components for velocity field fitting and integration  
515 are implemented in ITK, and the complete workflow is accessible in both ANTsPy  
516 (`ants.fit_time_varying_transform_to_point_sets(...)`) and ANTsR. In addition  
517 the availability of the DevCCF use case, self-contained examples and usage tutorials are  
518 provided in our public codebase.

## 519 4.5 Automated brain extraction and parcellation with ANTsXNet

520 To support template-based deep learning approaches for structural brain extraction and par-  
521 cellation, we implemented dedicated pipelines using the ANTsXNet framework. ANTsXNet  
522 comprises open-source deep learning libraries in both Python (ANTsPyNet) and R (ANTsR-  
523 Net) that interface with the broader ANTsX ecosystem and are built on TensorFlow/Keras.  
524 Our mouse brain pipelines mirror existing ANTsXNet tools for human imaging but are  
525 adapted for species-specific anatomical variation, lower SNR, and heterogeneous acquisition  
526 protocols.

### 527 4.5.1 Deep learning training setup

528 All networks were implemented in ANTsPyNet using standard 3D U-net architectures<sup>87</sup> pre-  
529 viously employed in previously published work<sup>44</sup>. Training was performed on an NVIDIA  
530 DGX system (4 × Tesla V100 GPUs, 256 GB RAM). Model weights and preprocessing  
531 routines are shared across ANTsPyNet and ANTsRNet to ensure reproducibility and lan-  
532 guage portability. For both published and unpublished trained networks available through  
533 ANTsXNet, all training scripts and data augmentation generators are publicly available at  
534 <https://github.com/ntustison/ANTsXNetTraining>.

535 **Data augmentation.** Robust data augmentation was critical to generalization across scan-  
536 ners, contrast types, and resolutions. We applied both intensity- and shape-based augmen-  
537 tation strategies:

538 • *Intensity augmentations:*

539 – Gaussian, Poisson, and salt-and-pepper noise:

540 `ants.add_noise_to_image(...)`

541 – Simulated intensity inhomogeneity via bias field modeling<sup>50</sup>:

542 `antspynet.simulate_bias_field(...)`

543 – Histogram warping to simulate contrast variation<sup>88</sup>:

544 `antspynet.histogram_warp_image_intensities(...)`

545 • *Shape augmentations:*

546 – Random nonlinear deformations and affine transforms:

547 `antspynet.randomly_transform_image_data(...)`

548 – Anisotropic resampling across axial, sagittal, and coronal planes:

549 `ants.resample_image(...)`

550 **4.5.2 Brain extraction**

551 We originally trained a mouse-specific brain extraction model on two manually masked  
552 T2-weighted templates, generated from public datasets<sup>66,67</sup>. One of the templates was  
553 constructed from orthogonal 2D acquisitions using B-spline-based volumetric synthesis via  
554 `ants.fit_bspline_object_to_scattered_data(...)`. Normalized gradient magnitude  
555 was used as a weighting function to emphasize boundaries during reconstruction<sup>85</sup>.

556 This training strategy provides strong spatial priors despite limited data by leveraging high-  
557 quality template images and aggressive augmentation to mimic population variability. Dur-  
558 ing the development of this work, the network was further refined through community en-  
559 gagement. A user from a U.S.-based research institute applied the publicly available (but  
560 then unpublished) brain extraction tool to their own mouse MRI dataset. Based on feedback

561 and iterative collaboration with the ANTsX team, the model was retrained and improved to  
562 better generalize to additional imaging contexts. This reflects our broader commitment to  
563 community-driven development and responsiveness to user needs across diverse mouse brain  
564 imaging scenarios.

565 The final trained network is available via ANTsXNet through the function  
566 `antspynet.mouse_brain_extraction(...)`. Additionally, both template/mask pairs are  
567 accessible via ANTsXNet. For example, one such image pair is available via:

- Template:

```
antspynet.get_antsxnet_data("bsplineT2MouseTemplate")
```

- Brain mask:

```
antspynet.get_antsxnet_data("bsplineT2MouseTemplateBrainMask")
```

#### 572 4.5.3 Brain parcellation

573 For brain parcellation, we trained a 3D U-net model using the DevCCF P56 T2-weighted  
574 template and anatomical segmentations derived from AllenCCFv3. This template-based  
575 training strategy enables the model to produce accurate, multi-region parcellations without  
576 requiring large-scale annotated subject data.

577 To normalize intensity across specimens, input images were preprocessed using rank-based  
578 intensity normalization (`ants.rank_intensity(...)`). Spatial harmonization was achieved  
579 through affine and deformable alignment of each extracted brain to the P56 template prior  
580 to inference. In addition to the normalized image input, the network also receives prior  
581 probability maps derived from the atlas segmentations, providing additional spatial context.

582 This general parcellation deep learning framework has also been applied in collaboration  
583 with other groups pursuing related but distinct projects. In one case, a model variant was  
584 adapted for T2-weighted MRI using an alternative anatomical labeling scheme; in another,  
585 a separate model was developed for serial two-photon tomography (STPT) with a different  
586 parcellation set. All three models are accessible through a shared interface in ANTsXNet:

`587 antspynet.mouse_brain_parcellation(...).` Ongoing work is further extending this ap-  
588 proach to embryonic mouse brain data. These independent efforts reflect broader community  
589 interest in adaptable parcellation tools and reinforce the utility of ANTsXNet as a platform  
590 for reproducible, extensible deep learning workflows.

`591 4.5.4 Evaluation and reuse`

`592 To assess model generalizability, both the brain extraction and parcellation networks were`  
593 `evaluated on an independent longitudinal dataset comprising multiple imaging sessions with`  
594 `varied acquisition parameters68.` Although each label or imaging modality required re-  
595 training, the process was streamlined by the reusable ANTsX infrastructure enabled by  
596 rapid adaptation with minimal overhead. These results illustrate the practical benefits of a  
597 template-based, low-shot strategy and modular deep learning framework. All trained mod-  
598 els, associated training scripts, and supporting resources are openly available and designed  
599 for straightforward integration into ANTsX workflows.

600 **Data availability**

601 All data and software used in this work are publicly available. The DevCCF atlas is  
602 available at <https://kimlab.io/brain-map/DevCCF/>. ANTsPy, ANTsR, ANTsPyNet, and  
603 ANTsRNet are available through GitHub at the ANTsX Ecosystem (<https://github.com/>  
604 [ANTsX](#)). Training scripts for all deep learning functionality in ANTsXNet can also be  
605 found on GitHub (<https://github.com/ntustison/ANTsXNetTraining>). A GitHub reposi-  
606 tory specifically pertaining to the AllenCCFv3 mapping is available at <https://github.com/>  
607 [dontminchenit/CCFAAlignmentToolkit](#). For the other two contributions contained in this  
608 work, the longitudinal DevCCF mapping and mouse cortical thickness pipeline, we refer the  
609 interested reader to <https://github.com/ntustison/ANTsXMouseBrainMapping>.

610 **Acknowledgments**

611 Support for the research reported in this work includes funding from the National Institute  
612 of Biomedical Imaging and Bioengineering (R01-EB031722) and National Institute of Mental  
613 Health (RF1-MH124605 and U24-MH114827).

614 We also acknowledge the data contribution of Dr. Adam Raikes (GitHub @araikes) of the  
615 Center for Innovation in Brain Science at the University of Arizona for refining the weights  
616 of the mouse brain extraction network.

<sup>617</sup> **Author contributions**

<sup>618</sup> N.T., M.C., and J.G. wrote the main manuscript text and figures. M.C., M.K., R.D., S.S.,  
<sup>619</sup> Q.W., L.G., J.D., C.G., and J.G. developed the Allen registration pipelines. N.T. and F.K.  
<sup>620</sup> developed the time-varying velocity transformation model for the DevCCF. N.T. and M.T.  
<sup>621</sup> developed the brain parcellation and cortical thickness methodology. All authors reviewed  
<sup>622</sup> the manuscript.

623 **References**

- 624 1. Keller, P. J. & Ahrens, M. B. Visualizing whole-brain activity and development at  
the single-cell level using light-sheet microscopy. *Neuron* **85**, 462–83 (2015).
- 625 2. La Manno, G. *et al.* Molecular architecture of the developing mouse brain. *Nature*  
**596**, 92–96 (2021).
- 626 3. Wen, L. *et al.* Single-cell technologies: From research to application. *Innovation  
(Camb)* **3**, 100342 (2022).
- 627 4. Oh, S. W. *et al.* A mesoscale connectome of the mouse brain. *Nature* **508**, 207–14  
(2014).
- 628 5. Gong, H. *et al.* Continuously tracing brain-wide long-distance axonal projections in  
mice at a one-micron voxel resolution. *Neuroimage* **74**, 87–98 (2013).
- 629 6. Li, A. *et al.* Micro-optical sectioning tomography to obtain a high-resolution atlas of  
the mouse brain. *Science* **330**, 1404–8 (2010).
- 630 7. Ueda, H. R. *et al.* Tissue clearing and its applications in neuroscience. *Nat Rev  
Neurosci* **21**, 61–79 (2020).
- 631 8. Ståhl, P. L. *et al.* Visualization and analysis of gene expression in tissue sections by  
spatial transcriptomics. *Science* **353**, 78–82 (2016).
- 632 9. Burgess, D. J. Spatial transcriptomics coming of age. *Nat Rev Genet* **20**, 317 (2019).
- 633 10. Hardwick, S. A. *et al.* Single-nuclei isoform RNA sequencing unlocks barcoded exon  
connectivity in frozen brain tissue. *Nature biotechnology* **40**, 1082–1092 (2022).
- 634 11. Hawrylycz, M. *et al.* A guide to the BRAIN initiative cell census network data  
ecosystem. *PLoS biology* **21**, e3002133 (2023).
- 635 12. Wang, Q. *et al.* The allen mouse brain common coordinate framework: A 3D reference  
atlas. *Cell* **181**, 936–953.e20 (2020).
- 636 13. Perens, J. *et al.* An optimized mouse brain atlas for automated mapping and quantification  
of neuronal activity using iDISCO+ and light sheet fluorescence microscopy.  
*Neuroinformatics* **19**, 433–446 (2021).
- 637 14. Ma, Y. *et al.* A three-dimensional digital atlas database of the adult C57BL/6J mouse  
brain by magnetic resonance microscopy. *Neuroscience* **135**, 1203–1215 (2005).

- 638 15. Qu, L. *et al.* Cross-modal coherent registration of whole mouse brains. *Nature Methods* **19**, 111–118 (2022).
- 639 16. Kronman, F. N. *et al.* Developmental mouse brain common coordinate framework. *Nat Commun* **15**, 9072 (2024).
- 640 17. Chuang, N. *et al.* An MRI-based atlas and database of the developing mouse brain. *Neuroimage* **54**, 80–89 (2011).
- 641 18. Dries, R. *et al.* Advances in spatial transcriptomic data analysis. *Genome research* **31**, 1706–1718 (2021).
- 642 19. Ricci, P. *et al.* Removing striping artifacts in light-sheet fluorescence microscopy: A review. *Progress in biophysics and molecular biology* **168**, 52–65 (2022).
- 643 20. Agarwal, N., Xu, X. & Gopi, M. Robust registration of mouse brain slices with severe histological artifacts. in *Proceedings of the tenth indian conference on computer vision, graphics and image processing* 1–8 (2016).
- 644 21. Agarwal, N., Xu, X. & Gopi, M. Automatic detection of histological artifacts in mouse brain slice images. in *Medical computer vision and bayesian and graphical models for biomedical imaging: MICCAI 2016 international workshops, MCV and BAMBI, athens, greece, october 21, 2016, revised selected papers* 8 105–115 (Springer, 2017).
- 645 22. Tward, D. *et al.* 3d mapping of serial histology sections with anomalies using a novel robust deformable registration algorithm. in *International workshop on multimodal brain image analysis* 162–173 (Springer, 2019).
- 646 23. Cahill, L. S. *et al.* Preparation of fixed mouse brains for MRI. *Neuroimage* **60**, 933–939 (2012).
- 647 24. Sunkin, S. M. *et al.* Allen brain atlas: An integrated spatio-temporal portal for exploring the central nervous system. *Nucleic acids research* **41**, D996–D1008 (2012).
- 648 25. Kim, Y. *et al.* Brain-wide maps reveal stereotyped cell-type-based cortical architecture and subcortical sexual dimorphism. *Cell* **171**, 456–469 (2017).
- 649 26. Fürth, D. *et al.* An interactive framework for whole-brain maps at cellular resolution. *Nat Neurosci* **21**, 139–149 (2018).

- 650 27. Li, Y. *et al.* mBrainAligner-web: A web server for cross-modal coherent registration  
of whole mouse brains. *Bioinformatics* **38**, 4654–4655 (2022).
- 651 28. Puchades, M. A., Csucs, G., Ledergerber, D., Leergaard, T. B. & Bjaalie, J. G. Spatial  
registration of serial microscopic brain images to three-dimensional reference atlases  
with the QuickNII tool. *PloS one* **14**, e0216796 (2019).
- 652 29. Eastwood, B. S. *et al.* Whole mouse brain reconstruction and registration to a ref-  
erence atlas with standard histochemical processing of coronal sections. *Journal of  
Comparative Neurology* **527**, 2170–2178 (2019).
- 653 30. Ni, H. *et al.* A robust image registration interface for large volume brain atlas. *Sci  
Rep* **10**, 2139 (2020).
- 654 31. Pallast, N. *et al.* Processing pipeline for atlas-based imaging data analysis of struc-  
tural and functional mouse brain MRI (AIDAmri). *Front Neuroinform* **13**, 42 (2019).
- 655 32. Celestine, M., Nadkarni, N. A., Garin, C. M., Bougacha, S. & Dhenain, M. **Sammbar-  
MRI**: A library for processing SmAll-MaMmal BrAin MRI data in python. *Front  
Neuroinform* **14**, 24 (2020).
- 656 33. Ioanas, H.-I., Marks, M., Zerbi, V., Yanik, M. F. & Rudin, M. An optimized regis-  
tration workflow and standard geometric space for small animal brain imaging. *Neu-  
roimage* **241**, 118386 (2021).
- 657 34. Aggarwal, M., Zhang, J., Miller, M. I., Sidman, R. L. & Mori, S. Magnetic resonance  
imaging and micro-computed tomography combined atlas of developing and adult  
mouse brains for stereotaxic surgery. *Neuroscience* **162**, 1339–1350 (2009).
- 658 35. Chandrashekhar, V. *et al.* CloudReg: Automatic terabyte-scale cross-modal brain  
volume registration. *Nature methods* **18**, 845–846 (2021).
- 659 36. Jin, M. *et al.* SMART: An open-source extension of WholeBrain for intact mouse  
brain registration and segmentation. *eNeuro* **9**, (2022).
- 660 37. Negwer, M. *et al.* FriendlyClearMap: An optimized toolkit for mouse brain mapping  
and analysis. *Gigascience* **12**, (2022).
- 661 38. Lin, W. *et al.* Whole-brain mapping of histaminergic projections in mouse brain.  
*Proceedings of the National Academy of Sciences* **120**, e2216231120 (2023).

- 662 39. Zhang, M. *et al.* Spatially resolved cell atlas of the mouse primary motor cortex by MERFISH. *Nature* **598**, 137–143 (2021).
- 663 40. Shi, H. *et al.* Spatial atlas of the mouse central nervous system at molecular resolution. *Nature* **622**, 552–561 (2023).
- 664 41. Zhang, Y. *et al.* Reference-based cell type matching of *in situ* image-based spatial transcriptomics data on primary visual cortex of mouse brain. *Scientific Reports* **13**, 9567 (2023).
- 665 42. Klein, S., Staring, M., Murphy, K., Viergever, M. A. & Pluim, J. P. W. [Elastix: A toolbox for intensity-based medical image registration](#). *IEEE Trans Med Imaging* **29**, 196–205 (2010).
- 666 43. Fedorov, A. *et al.* 3D slicer as an image computing platform for the quantitative imaging network. *Magnetic resonance imaging* **30**, 1323–1341 (2012).
- 667 44. Tustison, N. J. *et al.* [The ANTsX ecosystem for quantitative biological and medical imaging](#). *Sci Rep* **11**, 9068 (2021).
- 668 45. Pagani, M., Damiano, M., Galbusera, A., Tsafaris, S. A. & Gozzi, A. Semi-automated registration-based anatomical labelling, voxel based morphometry and cortical thickness mapping of the mouse brain. *Journal of neuroscience methods* **267**, 62–73 (2016).
- 669 46. Anderson, R. J. *et al.* [Small animal multivariate brain analysis \(SAMBA\) - a high throughput pipeline with a validation framework](#). *Neuroinformatics* **17**, 451–472 (2019).
- 670 47. Allan Johnson, G. *et al.* Whole mouse brain connectomics. *Journal of Comparative Neurology* **527**, 2146–2157 (2019).
- 671 48. Yao, Z. *et al.* [A high-resolution transcriptomic and spatial atlas of cell types in the whole mouse brain](#). *Nature* **624**, 317–332 (2023).
- 672 49. Avants, B. B., Epstein, C. L., Grossman, M. & Gee, J. C. [Symmetric diffeomorphic image registration with cross-correlation: Evaluating automated labeling of elderly and neurodegenerative brain](#). *Med Image Anal* **12**, 26–41 (2008).
- 673 50. Tustison, N. J. *et al.* [N4ITK: Improved N3 bias correction](#). *IEEE Trans Med Imaging* **29**, 1310–20 (2010).

- 674 51. Bajcsy, R. & Broit, C. Matching of deformed images. in *Sixth International Conference on Pattern Recognition (ICPR'82)* 351–353 (1982).
- 675 52. Bajcsy, R. & Kovacic, S. [Multiresolution elastic matching](#). *Computer Vision, Graphics, and Image Processing* **46**, 1–21 (1989).
- 676 53. Gee, J. C., Reivich, M. & Bajcsy, R. [Elastically deforming 3D atlas to match anatomical brain images](#). *J Comput Assist Tomogr* **17**, 225–36 (1993).
- 677 54. Klein, A. *et al.* [Evaluation of 14 nonlinear deformation algorithms applied to human brain MRI registration](#). *Neuroimage* **46**, 786–802 (2009).
- 678 55. Murphy, K. *et al.* [Evaluation of registration methods on thoracic CT: The EMPIRE10 challenge](#). *IEEE Trans Med Imaging* **30**, 1901–20 (2011).
- 679 56. Baheti, B. *et al.* [The brain tumor sequence registration challenge: Establishing correspondence between pre-operative and follow-up MRI scans of diffuse glioma patients](#). (2021).
- 680 57. Avants, B. B. *et al.* [The optimal template effect in hippocampus studies of diseased populations](#). *Neuroimage* **49**, 2457–66 (2010).
- 681 58. Avants, B. B., Tustison, N. J., Wu, J., Cook, P. A. & Gee, J. C. [An open source multivariate framework for n-tissue segmentation with evaluation on public data](#). *Neuroinformatics* **9**, 381–400 (2011).
- 682 59. Manjón, J. V., Coupé, P., Martí-Bonmatí, L., Collins, D. L. & Robles, M. [Adaptive non-local means denoising of MR images with spatially varying noise levels](#). *J Magn Reson Imaging* **31**, 192–203 (2010).
- 683 60. Wang, H. *et al.* [Multi-atlas segmentation with joint label fusion](#). *IEEE Trans Pattern Anal Mach Intell* **35**, 611–23 (2013).
- 684 61. Tustison, N. J. *et al.* Optimal symmetric multimodal templates and concatenated random forests for supervised brain tumor segmentation (simplified) with ANTsR. *Neuroinformatics* (2014) doi:10.1007/s12021-014-9245-2.

- 685 62. Tustison, N. J., Yang, Y. & Salerno, M. [Advanced normalization tools for cardiac motion correction](#). in *Statistical atlases and computational models of the heart - imaging and modelling challenges* (eds. Camara, O. et al.) vol. 8896 3–12 (Springer International Publishing, 2015).
- 686 63. McCormick, M., Liu, X., Jomier, J., Marion, C. & Ibanez, L. [ITK: Enabling reproducible research and open science](#). *Front Neuroinform* **8**, 13 (2014).
- 687 64. Beg, M. F., Miller, M. I., Trouvé, A. & Younes, L. [Computing large deformation metric mappings via geodesic flows of diffeomorphisms](#). *International Journal of Computer Vision* **61**, 139–157 (2005).
- 688 65. Tustison, N. J. & Avants, B. B. [Explicit B-spline regularization in diffeomorphic image registration](#). *Front Neuroinform* **7**, 39 (2013).
- 689 66. Hsu, L.-M. *et al.* CAMRI mouse brain MRI data.
- 690 67. Reshetnikov, V. *et al.* High-resolution MRI data of brain C57BL/6 and BTBR mice in three different anatomical views.
- 691 68. Rahman, N., Xu, K., Budde, M. D., Brown, A. & Baron, C. A. [A longitudinal microstructural MRI dataset in healthy C57Bl/6 mice at 9.4 tesla](#). *Sci Data* **10**, 94 (2023).
- 692 69. Liu, J. *et al.* [Concordance of MERFISH spatial transcriptomics with bulk and single-cell RNA sequencing](#). *Life Sci Alliance* **6**, (2023).
- 693 70. Stringer, C., Wang, T., Michaelos, M. & Pachitariu, M. [Cellpose: A generalist algorithm for cellular segmentation](#). *Nat Methods* **18**, 100–106 (2021).
- 694 71. Jia, H., Yap, P.-T., Wu, G., Wang, Q. & Shen, D. Intermediate templates guided groupwise registration of diffusion tensor images. *NeuroImage* **54**, 928–939 (2011).
- 695 72. Tang, S., Fan, Y., Wu, G., Kim, M. & Shen, D. RABBIT: Rapid alignment of brains by building intermediate templates. *NeuroImage* **47**, 1277–1287 (2009).
- 696 73. Dewey, B. E., Carass, A., Blitz, A. M. & Prince, J. L. Efficient multi-atlas registration using an intermediate template image. in *Proceedings of SPIE—the international society for optical engineering* vol. 10137 (NIH Public Access, 2017).

- 697 74. Perens, J. *et al.* Multimodal 3D mouse brain atlas framework with the skull-derived  
coordinate system. *Neuroinformatics* **21**, 269–286 (2023).
- 698 75. Rotolo, T., Smallwood, P. M., Williams, J. & Nathans, J. Genetically-directed, cell  
type-specific sparse labeling for the analysis of neuronal morphology. *PLoS One* **3**,  
e4099 (2008).
- 699 76. Peng, H. *et al.* Morphological diversity of single neurons in molecularly defined cell  
types. *Nature* **598**, 174–181 (2021).
- 700 77. Gong, H. *et al.* High-throughput dual-colour precision imaging for brain-wide connec-  
tome with cytoarchitectonic landmarks at the cellular level. *Nat Commun* **7**, 12142  
(2016).
- 701 78. Wang, J. *et al.* Divergent projection patterns revealed by reconstruction of individual  
neurons in orbitofrontal cortex. *Neurosci Bull* **37**, 461–477 (2021).
- 702 79. Kronman, F. A. *et al.* Developmental mouse brain common coordinate framework.  
*bioRxiv* (2023) doi:[10.1101/2023.09.14.557789](https://doi.org/10.1101/2023.09.14.557789).
- 703 80. Chon, U., Vanselow, D. J., Cheng, K. C. & Kim, Y. Enhanced and unified anatomical  
labeling for a common mouse brain atlas. *Nat Commun* **10**, 5067 (2019).
- 704 81. Tasic, B. *et al.* Adult mouse cortical cell taxonomy revealed by single cell transcript-  
omics. *Nat Neurosci* **19**, 335–46 (2016).
- 705 82. Bergmann, E., Gofman, X., Kavushansky, A. & Kahn, I. Individual variability in  
functional connectivity architecture of the mouse brain. *Commun Biol* **3**, 738 (2020).
- 706 83. Billot, B. *et al.* SynthSeg: Segmentation of brain MRI scans of any contrast and  
resolution without retraining. *Med Image Anal* **86**, 102789 (2023).
- 707 84. Rolfe, S. M., Whikehart, S. M. & Maga, A. M. Deep learning enabled multi-organ  
segmentation of mouse embryos. *Biol Open* **12**, bio059698 (2023).
- 708 85. Tustison, N. J. & Amini, A. A. Biventricular myocardial strains via nonrigid registra-  
tion of anatomical NURBS model [corrected]. *IEEE Trans Med Imaging* **25**, 94–112  
(2006).
- 709 86. Avants, B. B. *et al.* The Insight ToolKit image registration framework. *Front Neu-  
roinform* **8**, 44 (2014).

- 710 87. Falk, T. *et al.* U-net: Deep learning for cell counting, detection, and morphometry. *Nat Methods* **16**, 67–70 (2019).
- 711 88. Tustison, N. J. *et al.* Image- versus histogram-based considerations in semantic segmentation of pulmonary hyperpolarized gas images. *Magn Reson Med* **86**, 2822–2836 (2021).